JOURNAL OF OPTOELECTRONICS AND ADVANCED MATERIALS Vol. 10, No. 10, October 2008, p. 2547 - 2554

Large area InGaAs/GaAs resonant cavity enhanced photodetector for sensor application

B. K. JEONG, Y.M. SONG, V.V. LYSAK, Y. T. LEE*
Gwangju Institute of Science and Technology, Gwangju, Republic of Korea

This study deals with the fabrication and characterization of large area InGaAs/GaAs resonant cavity enhanced photodetector (RCEPD) based on intra-cavity 980 nm vertical cavity surface emitting laser (VCSEL) structure for sensor applications. To incorporate RCEPDs for sensor applications, RCEPD's with reasonable full width half maximum (FWHM) and high quantum efficiency are necessary. Therefore, we designed symmetric and asymmetric contact layer structure RCEPD's having 5 top DBR pairs and different sensitive area sizes. Asymmetric contact layer structure RCEPD showed slightly higher quantum efficiency, reduced FWHM, reduced 3dB bandwidth and a higher resistance than that of symmetric contact layer structure RCEPD.

(Received April 10, 2008; accepted August 14, 2008)

Keywords: Resonant cavity enhanced photodetector, RCEPD, InGaAs/GaAs photodetector, Large sensitive area

1. Introduction

A photodetector, which converts the detected photons to electrical signal, is a key component in optical transmission and optical measurement systems. High sensitivity, fast response, low noise, low cost, and high reliability are some of the basic requirements for a photodetector. A p-i-n photodetector has been used since it can meet most of the above mentioned characteristics. However, the main drawback of conventional p-i-n photodetector is the trade-off between quantum efficiency and response speed. For example, quantum efficiency of 100 % can be achieved by increasing the thickness of i-layer. However, it takes a long time for carriers to drift across the depletion region due to the thick i-layer region. This means that high quantum efficiency and high response speed can not be achieved, simultaneously.

Several techniques have been developed to improve the quantum efficiency of high speed photodetector. In one approach, resonant cavity enhanced photodetector (RCEPD) has been demonstrated as a novel device, which can achieve high quantum efficiency and high response speed, simultaneously [1]. The thin absorbing region is placed inside a Fabry-Perot cavity. The top and bottom mirror of this cavity, which formed by quarter-wave stacks of GaAs/AlGaAs, allows incident light to have more than one absorbing path inside the active region [1-3]. Due to multiple reflections, nearly 100 % quantum efficiency can be achieved in RCEPD. This means that a very thin absorbing region can achieve a high quantum efficiency as well as high response speed. However, high quantum efficiency can lead to the narrow spectral characteristic.

RCEPDs are promising devices for free-space optical communication, optical interconnects, metrology and optical sensing applications. In addition, the possibility of monolithic integration of vertical cavity surface emitting laser (VCSEL) and RCEPD can be used for integrated fluorescence sensing system [4, 5]. A major advantage of using VCSEL sources together with RCEPD based on VCSEL structure on a chip is that the same processing steps can be used for fabricating these devices, which makes this combination highly attractive for low cost integrated applications [6,7].

In previous papers [8-10] we have shown how to optimize the high speed intracavity contacted oxide confined VCSELs.

To realize these kinds of applications, RCEPD's with reasonable full width half maximum (FWHM) and high quantum efficiency are necessary. Our target was to make a RCEPD having FWHM ≥ 2 nm and quantum efficiency ≥ 50 % for the appropriate sensor applications. Therefore, RCEPD having 5 pairs top DBR were fabricated and their characteristics were measured.

2. Theoretical modeling of RCEPD

2.1. Top and Bottom QWS Reflectivity

We assumed that whole media is homogeneous and plane wave is propagating in the xz plane. With reference to Fig. 1 for the RCEPD model, the top QWS dielectric profile is described by

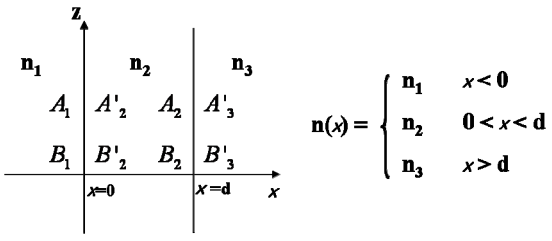

Fig. 1. Top and bottom reflectivity of RCEPD model

Let A_1 and B_1 be the amplitude of the incident and reflected plane wave at x=0, and A'_3 and B'_3 be the corresponding amplitudes at x=d.

These amplitude are related by the 2x2 transfer matrix M_1 [11]. Thus,

$$\begin{bmatrix} A_1 \\ B_1 \end{bmatrix} = M_1 \begin{bmatrix} A'_3 \\ B'_3 \end{bmatrix} \tag{1}$$

For the top QWS reflectivity, matrix M_1 is given by

$$M_1 = \begin{bmatrix} M_{11} & M_{12} \\ M_{21} & M_{22} \end{bmatrix} = D_1^{-1}[D_2 P_2(\lambda) D_2^{-1}]^{N_1} D_3 \tag{2}$$

where N_1 is the number of top pairs of layer and D_i is the dynamical matrix of layer i of refractive index n_i and width d_i. Matrix M_1 accounts for the change in the amplitude of the incident and reflected components of a wave on entry and exit from the medium. D_i is given by [11]

$$D_i = \begin{bmatrix} 1 & 1 \\ n_i \cos\theta_i & -n_i \cos\theta_i \end{bmatrix} \tag{3}$$

$P_i(\lambda)$ is the propagation matrix and it accounts for the phase change experienced by the wave after it has passed though the layer. It is given by [11]

$$P_i(\lambda) = \begin{bmatrix} e^{j\phi_i(\lambda)} & 0 \\ 0 & e^{j\phi_i(\lambda)} \end{bmatrix} \tag{4}$$

where

$$\Phi_i(\lambda) = n_i d_i \frac{2\pi}{\lambda} \cos\theta_i \tag{5}$$

The reflection coefficiency, which is defined as a function of the wavelength λ, can be express in terms of the elements of M_1 by

$$r_1(\lambda) = \frac{M_{21}}{M_{11}} \equiv \sqrt{R_1(\lambda)} e^{j\psi_1(\lambda)} \tag{6}$$

where the reflectivity of the top QWS is given by

$$R_1(\lambda) = |r_1(\lambda)|^2 \tag{7}$$

and

$$\psi_1(\lambda) = \arg[r_1(\lambda)] \tag{8}$$

For the bottom QWS reflectivity, matrix M_2 is given by

$$M_2 = \begin{bmatrix} M'_{11} & M'_{12} \\ M'_{21} & M'_{22} \end{bmatrix} = D_1^{-1}[D_2 P_2(\lambda) D_2^{-1}]^{N_2} D_3 \tag{9}$$

where N_2 is the number of bottom pairs of layer. The reflection coefficiency,

$$r_2(\lambda) = \frac{M'_{21}}{M'_{11}} \equiv \sqrt{R_2(\lambda)} e^{j\psi_2(\lambda)} \tag{10}$$

where the reflectivity of the bottom QWS is given by

$$R_2(\lambda) = |r_2(\lambda)|^2 \tag{11}$$

and

$$\psi_2(\lambda) = \arg[r_2(\lambda)] \tag{12}$$

2.2. Quantum efficiency

The quantum efficiency η of a photodetector is defined as the probability that a single photon incident on the device generates an electron hole pair which contributes to the detector current. Quantum efficiency can be calculated by using the RCEPD model shown in Fig. 2.

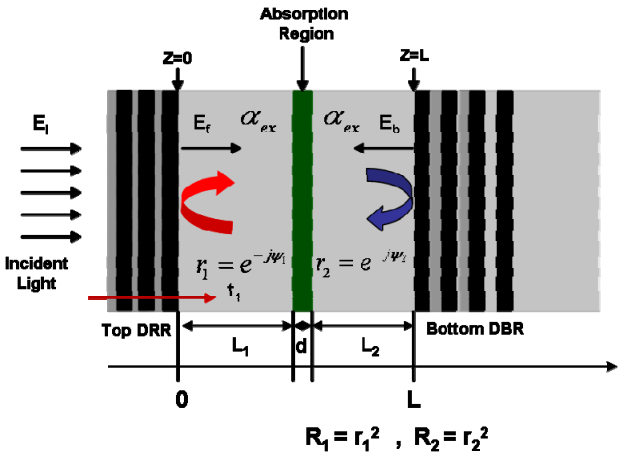

Fig. 2. Analysis model of RCEPD. The active region of thickness d is a small bandgap semiconductor. The top and bottom DBR mirrors consist of alternating layers of non-absorbing larger bandgap materials.

The field reflection coefficients of the top and bottom mirrors are denoted $r_1 e^{-j\psi_1}$ and $r_2 e^{-j\psi_2}$, respectively, where ψ_1 and ψ_2 donate phase shift due to light penetration into

the mirrors. The active layer, where absorption occurs, is placed between the two mirror structures and is defined by its thickness d and absorption coefficient α. The separation between the active layer and the top and the bottom mirrors respectively are indicated by L_1 and L_2. The absorption coefficient outside the active region is denoted α_{ex}. Quantum efficiency η is the ratio of the absorbed power to the incident optical power, i.e. $\eta = \frac{P_l}{P_i}$. Hence [1]:

$$\eta = \frac{(1+R_2 e^{-\alpha d})(1-R_1)(1-e^{-\alpha d})}{1-2\sqrt{R_1 R_2}e^{-\alpha d}\cos(2\beta L+\psi_1+\psi_2)+R_1 R_2 e^{-2\alpha d}} \qquad (13)$$

The peak η at the resonant wavelengths can be derived by imposing the resonant condition in (13)

$$\eta_{\max} = \frac{(1+R_2 e^{-\alpha d})}{(1-\sqrt{R_1 R_2}e^{-\alpha d})^2}(1-R_1)(1-e^{-\alpha d}) \qquad (14)$$

3. Device design, material growth and device fabrication

3.1. Device design

The goal of our research is to make a RCEPD having FWHM ≥ 2 nm and quantum efficiency ≥ 50 % [9]. According to theory, there is trade-off between quantum efficiency and FWHM [13]. To realize these characteristics (FWHM ≥ 2 nm, quantum efficiency ≥ 50 %), top DBR pairs should be etched to give a wide FWHM. Relationship between the number of top DBR pairs and quantum efficiency simulated and these indicate that 5 pairs top DBR are appropriate for meeting the RCEPD design specification. Simulated result is shown in Fig. 3.

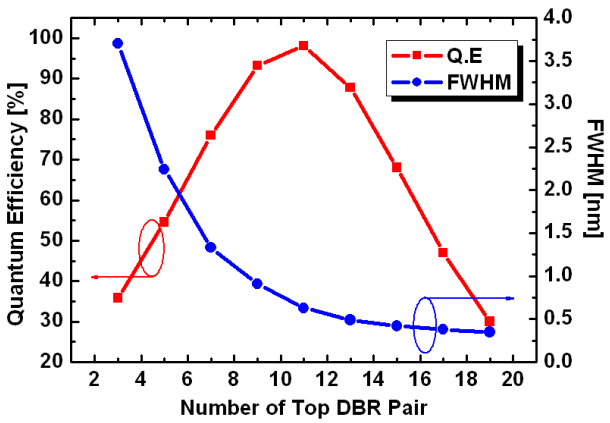

Fig. 3. Quantum efficiency and FWHM versus top DBR pairs.

Another design consideration is to give a uniform electric field distribution. As increasing sensitive area size, electric field may be reduced in the center of device as shown in Fig 4. It means that generated electron-hole pairs in the center of device can not reach the metal contact layer. This will reduce the responsivity. Therefore, asymmetric contact layer structure RCEPD design is implemented to give a uniform electric field distribution.

These structures are expected to increase the responsivity.

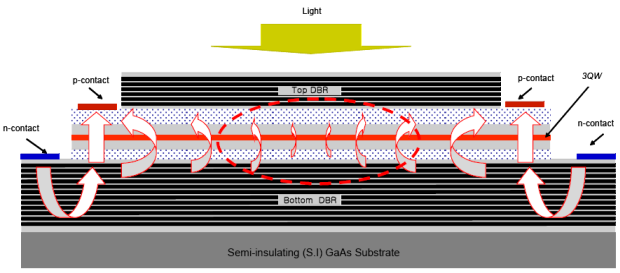

Fig. 4. Qualitative analysis of electric field distribution of symmetric contact layer structure RCEPD

3.2. Material growth

The epitaxial layer structure of designed RCEPD which used in this experiment is shown in Fig. 5. The RCEPD epitaxy was grown by molecular beam epitaxy (MBE) on semi-insulating GaAs (100) substrate [14]. The top and bottom DBR mirror consists of 5 and 30.5 pairs of quarter-wavelength thick GaAs-$Al_{0.88}Ga_{0.12}As$ layers, respectively. The resonator cavity consists of three 85 Å thick $In_{0.19}Ga_{0.81}As$ quantum well with 100Å thick GaAs barriers and centered in 1 λ cavity. The cavity is bounded on each side by p- and n-doped $Al_{0.98}Ga_{0.02}As$ oxidation layers followed by 7/4 λ-thick p- and 5/4 λ-thick n-doped GaAs contact layers. Both sides of the $Al_{0.98}Ga_{0.02}As$ oxidation layers were composition-graded in order to reduce the resistance. Both top and bottom DBR mirrors are designed to have a center wavelength at 980 nm. The reflectivity spectrum near the center of the grown RCEPD wafer is shown in Fig. 6. Fabry-Perot (FP) mode is positioned at 969.8 nm and photoluminescence (PL) emission of the InGaAs quantum wells is positioned at 966.8 nm, a 3 nm offset from the FP mode. The FP mode is often intentionally designed to be longer wavelength relative to the PL mode at room temperature. Because the PL mode red shifts rate is faster than the FP mode as the temperature increases.

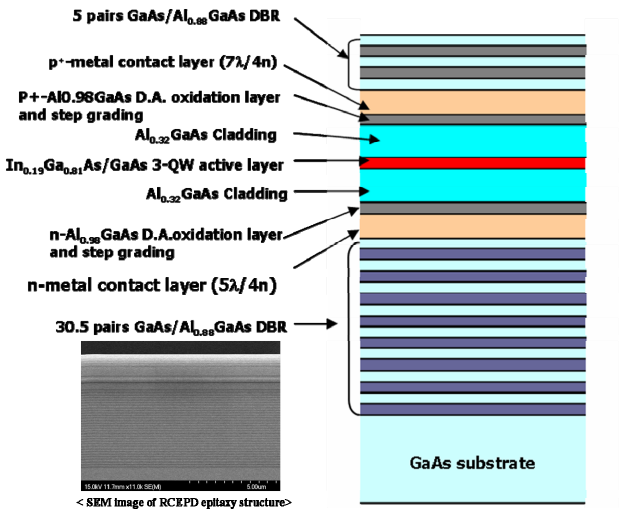

Fig. 5. Designed RCEPD epitaxy structure.

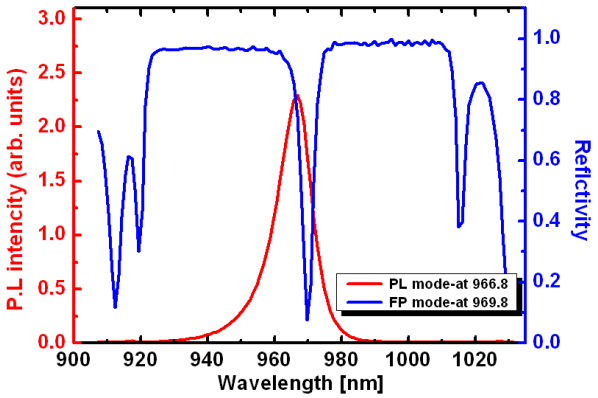

Fig. 6. Measured reflectivity spectrum of an as-grown RCEPD and PL spectrum after top DBR etching. FP mode and PL peaks are at 969.8 nm and 966.8 nm, respectively.

3.3. Device fabrication

The first step of RCEPD fabrication process is to expose the p-GaAs contact layer, second step is to expose the n-GaAs contact layer and third step is to provide isolation between etched devices. Passivation process is needed to protect the active layers and to get flatness for safe connection between a metal ring and a bonding pad. Then, Si_3N_4 was deposited to enhance adhesion of p-, n-metal bonding pad after BCB coating. After Si_3N_4 deposition, BCB should be deeply etched to expose p- and n-contact layer. Then, contact metallization and rapid thermal annealing (RTA) process are conducted. The final process is to open the sensitive area to detect the light. Fabricated cross section view of RCEPD is shown in Fig. 7.

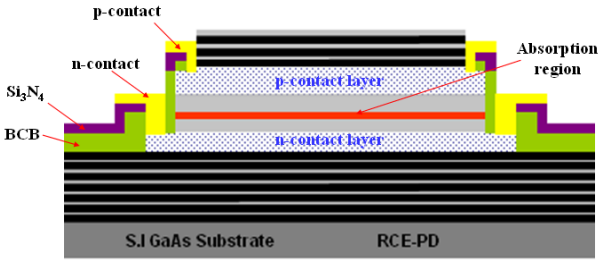

Fig. 7. Fabricated cross section view of RCEPD.

4. Characteristics and discussion

Here we will discuss the RCEPD characteristics such as dark current, capacitance, responsivity, photocurrent, and frequency response.

4.1. Dark current

Dark current was measured by a semiconductor parameter analyzer (Agilent 4156C) in the dark box at night. Several samples were measured to get reasonable results. The measured dark current of 80 um, 130 um and 210 um diameter RCEPD shown in Fig. 8 are 30.27 pA, 37.59 pA, and 52.64 pA at -3.3 V, respectively. These results indicate that RCEPD's dark current is much lower than that of commercial p-i-n photodetector. The main reason of low dark current is that the employment of very thin absorption layers provides a significant reduction of the generation component of the dark current [12]. Generally, dark current increases as the size of the sensitive area increases.

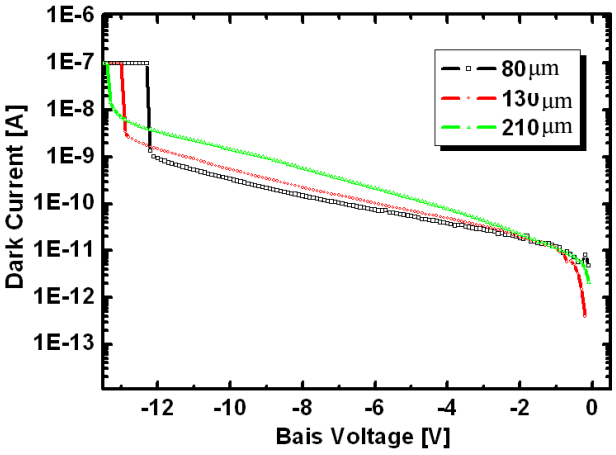

Fig. 8. Dark current as a function of voltage for device with different diameters.

4.2. Capacitance

The capacitance was measured by HP 4284A Precision LCR Meter equipment. Under reverse bias, junction capacitance is dominant, and is given by,

$$C = k_s \varepsilon_o \frac{A}{W} \tag{15}$$

where k_s is dielectric constant of undoped absorption layer $In_{0.2}GaAs$ (k_s =13.69), and W is transition length. Therefore, as the sensitive area (A) increases, the junction capacitance also increases. The measured capacitance is 4.82 pF, 5.64 pF, 7.47 pF and 9.58 pF for 80 um, 90 um, 110 um, and 130 um symmetric contact layer structure at -3.3 V, respectively. This value is much higher than that of commercial p-i-n photodetector due to short transition length (W). For the case of asymmetric contact layer structure device, there is no different from the symmetric contact layer structure. Fig. 9 shows the capacitance characteristics under reverse bias from -5 V to 0.5 V for the different sensitive area sizes.

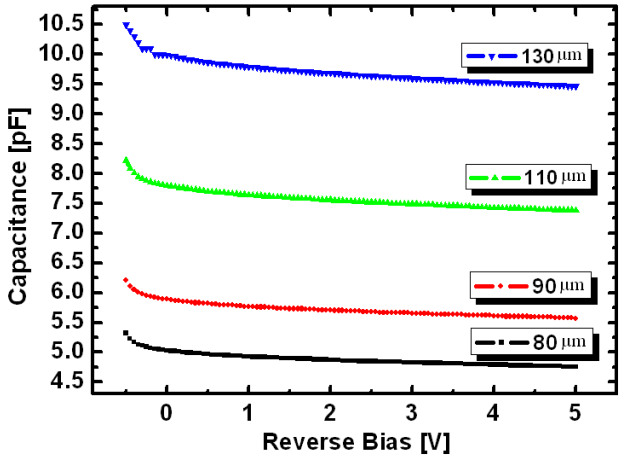

Fig. 9. Capacitance as a function of voltage for device with different diameters.

4.3. Photocurrent

The photocurrent was measured by using the responsivity setup in the dark box at night. For the symmetric case of 80 um diameter, the measured photocurrent is linearly increases as the incident optical power increases as shown in Fig. 10. The voltage at which photocurrent saturates is about -1 V.

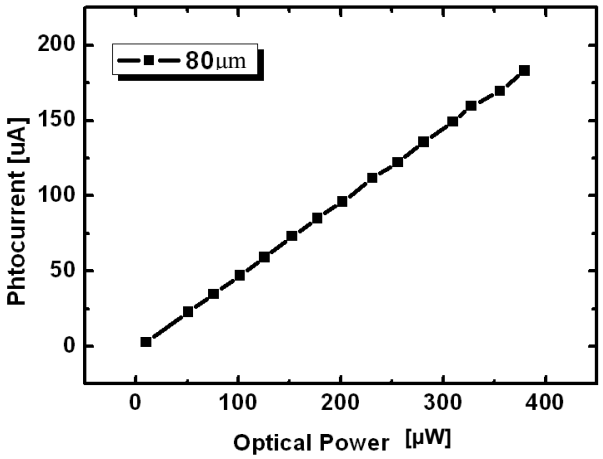

Fig. 10. Photocurrent for various incident powers for 80 μm diameter device for the symmetric case at -3.3 V.

4.4. Responsivity

The responsivity was measured by a 980 nm tunable external-cavity laser source (Toptica DL100), a semiconductor parameter analyzer (Agilent 4156C), an optical spectrum analyzer (Anritsu MS9710B), and a standard optical power meter (Newport) in the dark box at night. Fig. 11 shows the responsivity measurement setup. The 1 × 3 coupler divides light which from the tunable laser source into three parts. The optical spectrum analyzer detects wavelength and power meter reads the input power which goes into the RECPD. Parameter analyzer gives a bias voltage and detects the photocurrent.

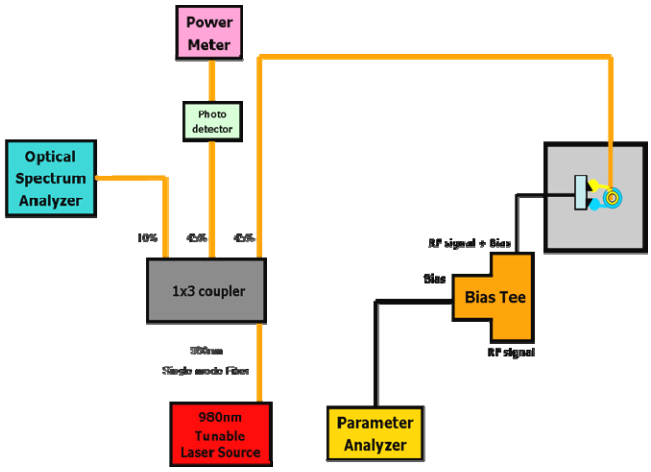

Fig. 11. Responsivity measurement setup

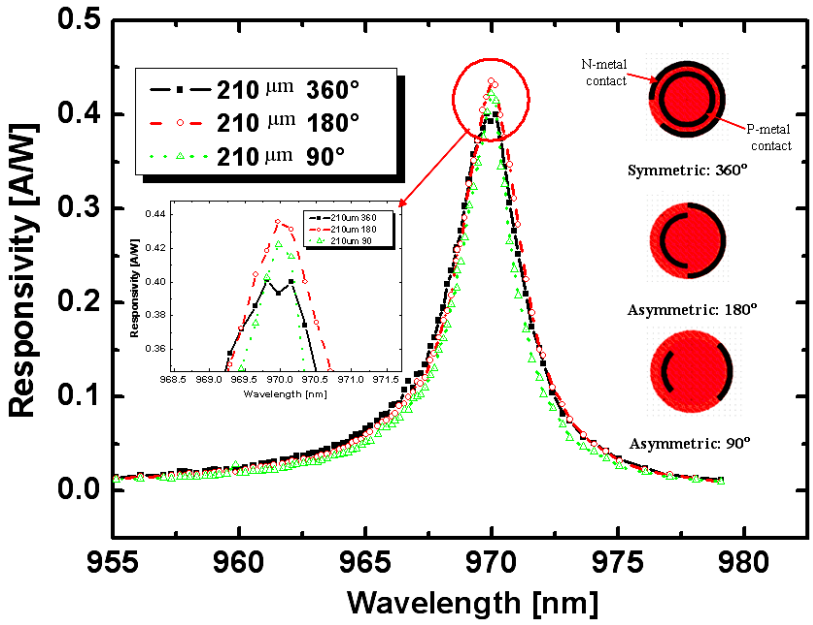

	Angle (°)	FWHM (nm)	Peak Lambda (nm)	Responsivity (A/W)	Quantum Efficiency (%)
Sensitive Area Diameter → 210um	360°	3.12	969.81	0.4013	51.31
	180°	2.76	969.97	0.4359	55.72
	90°	2.44	969.97	0.4224	54

Fig. 12. Responsivity of 210 μm diameter device for different contact layer structures at -3.3 V.

The measured responsivity and FWHM for 210 μm sensitive area devices shown in Fig. 12 are 3.12 nm and 0.4013 A/W for symmetric contact layer structure and 2.76 nm and 0.4359 A/W for asymmetric contact layer structure devices, respectively. These results show that responsivity of asymmetric contact layer structure devices was slightly improved. It means that electric field is enhanced in the center of device and this phenomenon is more prominent when the device has a large sensitive area size.

4.5. Frequency response

To study the frequency response, measured impulse response data for different diameter devices are converted to frequency domain using fast Fourier transform (FFT) [16]. The impulse response measurement setup is shown in Fig. 13.

It consists of a short pulse generator, LD driver, a 980 nm modulator, a semiconductor parameter analyzer (Agilent 4156C), a wide band oscilloscope (Agilent infiniium DCA 86100B), an optical spectrum analyzer (Anritsu MS9710B), and a standard optical power meter (Newport). Short pulse generator generates pulse, which has the pulse width of 50 ps and short pulse generator repetition rate is 10 MHz. LD driver gives bias current to 980 nm modulator.

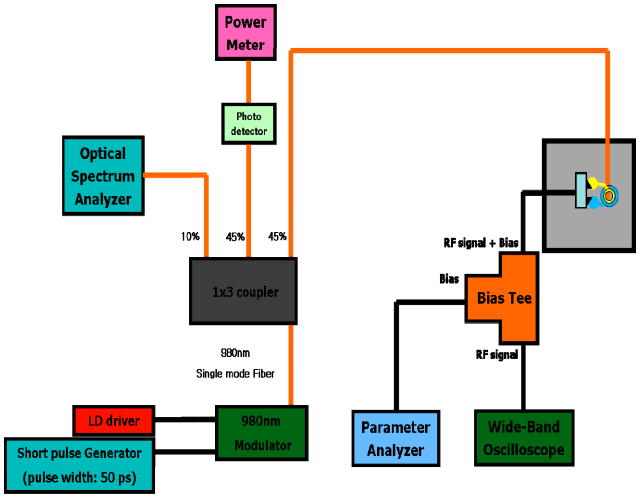

Fig. 13. Impulse response measurement setup

The 1 x 3 coupler divides light which from the 980 nm modulator into three parts. The optical spectrum analyzer detects wavelength and power meter reads the input power which goes into the RECPD. Parameter analyzer gives a bias voltage and detects the photocurrent. Wide band oscilloscope measures impulse response.

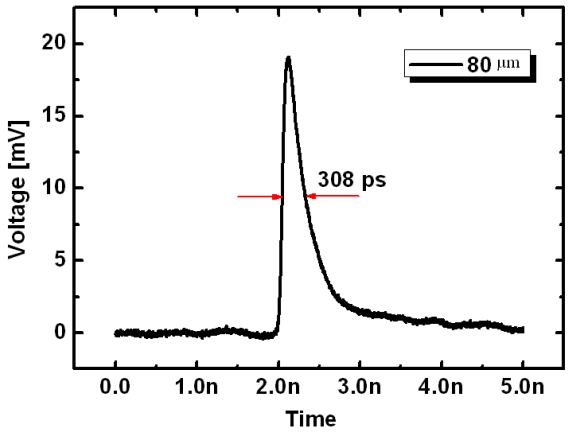

Fig. 14. (a) Reference signal: pulse width of 52.8 ps (b) Impulse response for 80 um symmetric case: pulse width of 308 ps at -3.3 V.

Fig. 14 shows that the reference impulse signal with pulse width of 52.8 ps and impulse response with a width of 308 ps at -3.3 V, which was measured for the 80 um symmetric contact layer structure device. A FFT was performed on the 80 um diameter symmetric contact layer structure device and obtained 3dB bandwidth is 1.32 GHz at -3.3 V as shown in Fig. 16.

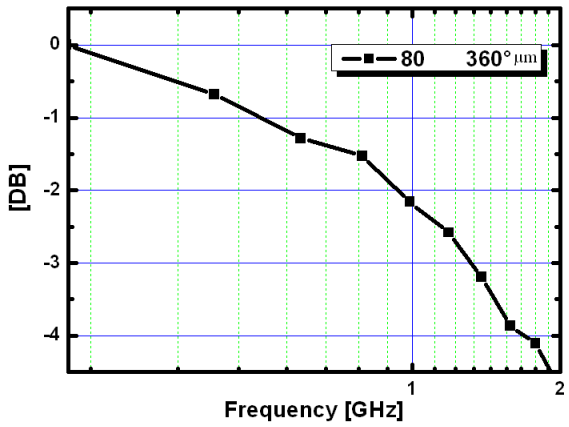

Fig. 16. Calibrated FFT for 80 μm diameter symmetric contact layer structure device at -3.3 V.

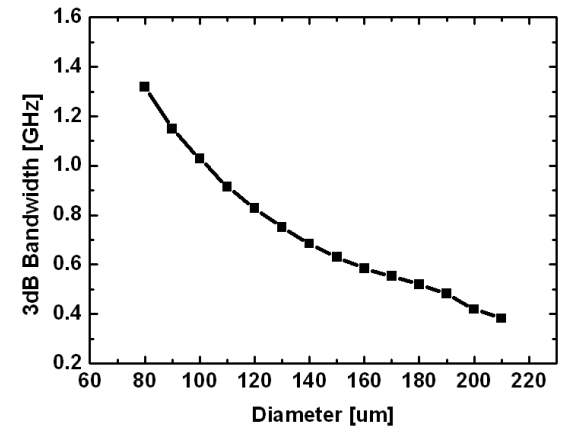

Fig. 17. Measured 3dB bandwidth as a function of diameter

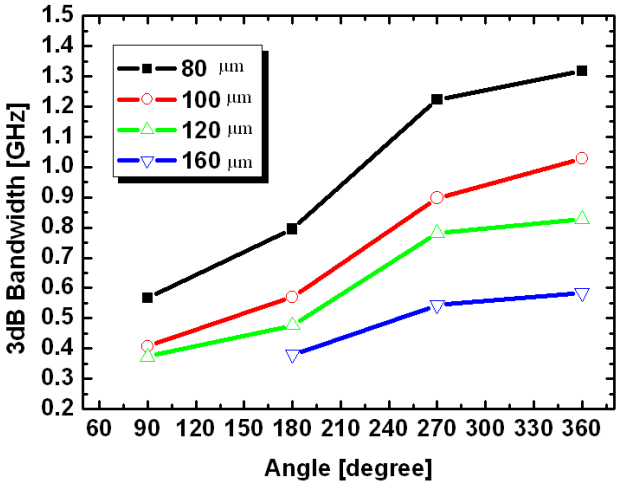

Fig. 18. 3dB bandwidth as a function of different contact layer structures

The measured 3dB bandwidth of RCEPD whose diameter ranges from an 80 μm to a 210 μm is shown in Fig. 17. These results indicate that 3dB bandwidth reduces as the sensitive area size increases due to large junction capacitance. Fig. 18 shows the 3dB bandwidth obtained from RECPD devices which diameter ranges from 80 um to 160 um diameter detectors for different contact layer structure at -3.3 V. As close to the symmetric contact layer structure devices, the 3dB bandwidth also increases because of the reduced resistance.

5. Conclusions

In this paper, designed RCEPD with 5 pairs top DBR was fabricated and their characteristics were analyzed. In addition, asymmetric contact layer structure RCEPD was also fabricated to give a uniform electric field distribution in the center of device in order to increase the responsivity.

Fabricated RCEPD characteristics are as follows:

- The measured dark current of 80 um diameter RCEPD is 30.27 pA at -3.3 V. This value is much lower than that of commercial p-i-n photodetector due to thinner absorption layers.
- The measured capacitance of 80 um diameter RCEPD is 4.82 pF at -3.3 V. This value is much higher than that of commercial p-i-n photodetector due to shorter transition length of RCEPD. For the case of asymmetric contact layer structure, there is no difference from the symmetric contact layer structure.
- Responsivity was slightly improved for the case of asymmetric contact layer structure. It means that electric field is enhanced in the center of devices, and this phenomenon is more prominent when the device has a large sensitive area.
- The measured saturation photocurrent linearly increases as the incident optical power increases and the voltage is about -1 V needed to saturate photocurrent.

- 3dB bandwidth reduces as the sensitive area size increases due to increased junction capacitance. For the 80 um symmetric contact layer device, 3dB bandwidth is 1.32 GHz at -3.3 V. In addition, as close to the symmetric contact layer structure, the 3dB bandwidth also increases because of lower resistance.

Acknowledgements

This work is supported by Schoold of Photonic Science and Technology and BK21 in Korea. The authors would like to thank Il-Sug Chung for helping to provide theoretical modeling methode of RCEPD. Ki-Soo Chang should be recognized for his effort in the device growth. Discussion with Sooraj.R and Jong-Min Kim are also acknowledged.

References

[1] M. Selim Unlu and Samuel Strite, Resonant Cavity Enhanced Photonic Devices, Journal of Applied Physics, **78,** 607 (1995).

[2] M. S. Unlu, K. Kishino, J. I. Chyi, J. Reed, S.N.Mohammad, and H. Morko Resonant cavity enhance GaAs/AlGaAs heterojunction phototransistor with intermediate InGaAs region in the collector, Appl. Phys. Lett. **57**, 750 (1990).

[3] A. Chin, T. Y. Chang, Enhancement of quantum efficiency in thin photodiodes through absorptive resonance, J. Lightwave Technol., **9** 321, (1991).

[4] E. Thrush, O. Levi, W. Ha, G. Carey, L. J. Cook, J. Deich, S. J. Smith, W. E Moerner and J. S. Harris, Jr., Integrated semiconductor vertical-cavity surface-emitting lasers and PIN photodetectors for bio-medical fluorescence sensing, IEEE J. Quantum Electronics, **40** 491, (2004).

[5] E. Thrush, O, Levi, W, Ha, Integrated bio-fluorescence sensor, Journal of Chromatography A**, 1,** 1013, (2003).

[6] O. Sjolund, D. A Louderback, E. R. Hegblom, J. Ko, L. A. Coldren Technique for integration of vertical cavity lasers and resonant photodetectors, Appl. Phys. Lett., **73** 1, (1998).

[7] D. A. Louderback, , et al., Modulation and Free-Space Link Characteristics of Monolithically Integrated Vertical-Cavity Lasers and Photodetectors with Microlenses, IEEE Journal of Selected Topics in Quantum Electronics, **5** 27, (1999).

[8] V. v. Lysak, Y. T. Lee, J. Optoelectron. Adv. Mater. **8**(4), 1601 (2006).

[9] V. V. Lysak, Ki Sva Chang, Y. T. Lee, J. Optoelectron. Adv. Mater. **8**(1), 355(2006).

[10] V. V. Lysak, K. S. Chang, Y. M. Song, Y. T. Lee, J. Optoelectron. Adv. Mater. **9**(9), 2813 (2007).

[11] P.Yen, Optical waves in Layered Media, New York, Wiley, (1988).

[12] M. Gokkavas, O. Dosunmu, and M. S. Unlu, High-Speed High-Efficiency Large-Area Resonant Cavity Enhanced p-i-n Photodiodes for Multimode Fiber Communications, IEEE Photonics Technology Letters, , **13** 1349, (2001).

[13] T. Knodl, H. K. H. Choy, J. L. Pan, R. King, R. Jäger, G. Lullo, J. F. Ahadian, R. J. Ram, C. G. Fonstad, Jr., and K. J. Ebeling, RCE photodetectors based on VCSEL structure, IEEE Photon. Technol. Lett. **11** 1289, (1999).

[14] K. S. Chang, J. M. Kim, J. D. Song, S. J. Bae, Y. T. Lee, B. J. Jeong, G. M. Yang, MBE growth of InGaAs/GaAs/AlGaAs VCSEL using in-situ optical reflectometry for pre-growth calibration, ISPSA 2002, **82**, (2002).

[15] B.N. Sverdlov, A.E. Botchkarev, N. Teraguchi, A.A. Salvador, and H. Morkoc, Resonant of dark current in photodiodes by the use of a resonant cavity, Electron. Lett. **29** 1019, (1993).

[16] I. S. Chung, J. K. Choi, Y. T. Lee, Intra-cavity-contacted resonant cavity photodetectors for high speed bi-directional optical interconnects, SPIE Symposium on Asia Pacific Optical Communications (APOC), 6352-62 , (2006).

* Corresponding author: ytlee@gist.ac.kr